STRUCTURAL BIOLOGY

Skp1 proteins are structural components of the synaptonemal complex in *C. elegans*

Joshua M. Blundon[1]†, Brenda I. Cesar[1]†, Jung Woo Bae[1], Ivana Čavka[2,3], Jocelyn Haversat[1], Jonas Ries[2], Simone Köhler[2], Yumi Kim[1]*

The synaptonemal complex (SC) is a zipper-like protein assembly that links homologous chromosomes to regulate recombination and segregation during meiosis. The SC has been notoriously refractory to in vitro reconstitution, thus leaving its molecular organization largely unknown. Here, we report a moonlighting function of two paralogous S-phase kinase-associated protein 1 (Skp1)–related proteins (SKR-1 and SKR-2), well-known adaptors of the Skp1–Cul1–F-box (SCF) ubiquitin ligase, as the key missing components of the SC in *Caenorhabditis elegans*. SKR proteins repurpose their SCF-forming interfaces to dimerize and interact with meiosis-specific SC proteins, thereby driving synapsis independent of SCF activity. SKR-1 enables the formation of the long-sought-after soluble complex with previously identified SC proteins in vitro, which we propose it to represent a complete SC building block. Our findings demonstrate how a conserved cell cycle regulator has been co-opted to interact with rapidly evolving meiotic proteins to construct the SC and provide a foundation for understanding its structure and assembly mechanisms.

INTRODUCTION

The synaptonemal complex (SC) is a hallmark of meiotic prophase and plays a crucial role in regulating crossovers between homologous chromosomes (*1*–*5*). The SC is conventionally viewed as a tripartite structure consisting of two parallel chromosome axes that organize chromatin into loops and a central region that links the paired homologs (*6*). Although the appearance of the SC is highly similar across eukaryotes, its components have diverged extensively (*7*, *8*). The SC central region in *Caenorhabditis elegans* is known to be composed of six coiled-coil domain proteins, SYP-1, SYP-2, SYP-3, SYP-4, and SYP-5/6, which are mutually dependent on each other for their chromosomal loading (*9*–*14*). While their interactions are mediated via their coiled-coil domains and charged sequence motifs embedded within them (*10*, *15*), the molecular organization and stoichiometry of the SYP proteins remain elusive. Previous attempts to purify the existing slate of SC proteins proved unsuccessful because of their insolubility, suggesting that additional missing factors may be necessary.

In recent studies in *C. elegans*, two paralogous Skp1-related (SKR) proteins, SKR-1 and SKR-2, have been found to associate with the SYP proteins (*9*, *10*). Skp1 is an adaptor of the Skp1–Cul1–F-box (SCF) ubiquitin ligase that mediates polyubiquitination of target proteins (Fig. 1A), thereby promoting their degradation by the proteasome (*16*). Depleting SCF subunits during meiosis leads to severe synapsis defects in fungi, plants, and animals (*17*–*25*), indicating a pervasive role of SCF in regulating SC assembly. In *C. elegans,* the SCF complex containing an F-box protein progression of meiosis (PROM)–1 (SCF^{PROM-1}) targets a Protein phosphatase 2C (PP2C) phosphatase Protein phosphatase 1D (PPM-1.D) for degradation during the transition from mitosis to meiosis, leading to activation of Checkpoint kinase 2 (CHK-2) kinase and initiation of meiotic chromosome dynamics (*26*–*28*). The SCF complex also controls pachytene exit in *C. elegans* and mediates the degradation of translational regulators for maturing oocytes (*29*, *30*). Intriguingly, SKR-1/2–depleted germlines exhibit an extended region of leptotene/zygotene stage nuclei (*31*), which is now known to reflect a delayed meiotic progression in response to synapsis defects (*11*, *12*). However, the requirement for SKR-1/2 in synapsis and crossover formation remains unknown in *C. elegans*. Here, we report an unexpected discovery that SKR proteins serve as structural components of the SC, independent of their canonical roles within the SCF ubiquitin ligase. SKR proteins repurpose the SCF-forming interfaces to interact with the SYP proteins and form the long-sought-after soluble protein complex in vitro, suggesting that the core set of SC components has now been identified in *C. elegans*. Our findings reveal how highly conserved Skp1 proteins have been co-opted to interact with rapidly evolving SC proteins to construct an essential meiotic scaffold.

RESULTS

SKR-1 and SKR-2 associate with SC components in *C. elegans*

C. elegans encodes two germline-enriched SKR genes, *skr-1* and *skr-2,* which reside next to each other within a 2.7-kb region on chromosome I. SKR-1 and SKR-2 proteins share 81% identity at the amino acid level (*31, 32*). A BLAST search using SKR-1/2 as queries finds a single high-confidence hit in related *Caenorhabditis* species, which are present in syntenic regions with the identical set of neighboring genes as *C. elegans skr-1/2* (fig. S1A). Therefore, *skr-1* and *skr-2* were likely born from a recent gene duplication event within the *C. elegans* lineage. Western blot analysis of the 3xFlag tag fused to the C termini of both SKR-1 and SKR-2 revealed that SKR-1 is more abundantly expressed than SKR-2 (fig. S1B), consistent with the essential role of *skr-1* in embryo development (*33*). Therefore, we infer that *skr-1* has been derived from the ancestral gene and study both SKR proteins interchangeably.

To gain insight into the function of SKR-1/2 during meiotic prophase, we then immunoprecipitated SKR-2::3×Flag from isolated germline nuclei and analyzed the proteins associated with SKR-2 by

[1]Department of Biology, Johns Hopkins University, Baltimore, MD 21218, USA. [2]The European Molecular Biology Laboratory, Heidelberg, Germany. [3]Collaboration for joint PhD degree between EMBL and Heidelberg University, Faculty of Biosciences, Heidelberg, Germany.
*Corresponding author. Email: yumi.kim@jhu.edu
†These authors contributed equally to this work.

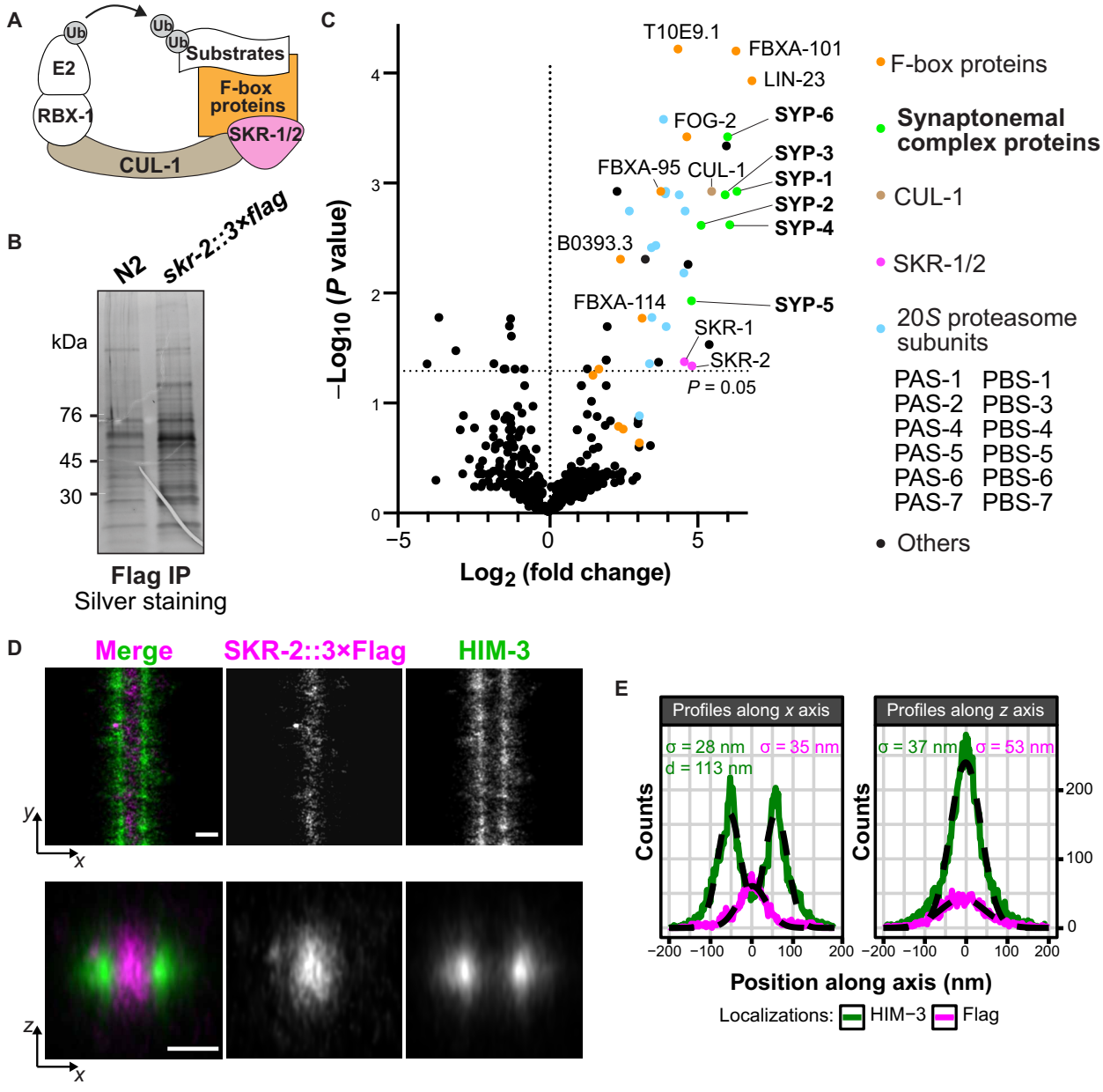

Fig. 1. SKR proteins associate with SC proteins and localize to the SC central region. (**A**) Schematic showing polyubiquitination of a substrate by an E2 ubiquitin-conjugating enzyme and the SCF ubiquitin ligase complex. RBX1, Ring-box protein 1. (**B**) A silver-stained SDS–polyacrylamide gel electrophoresis (PAGE) gel showing purified SKR-2–containing protein complexes using anti-Flag beads from a worm strain expressing SKR-2::3×Flag. N2 was used as a control. IP, immunoprecipitation. (**C**) A volcano plot showing proteins enriched in SKR-2 immunoprecipitates over N2 control. Normalized weighted spectra were transformed to logarithmic values (base 2) and analyzed by multiple unpaired *t* tests. The logarithm of fold change (base 2) is plotted on the *x* axis, and the negative logarithm of the *P* value (base 10) is plotted on the *y* axis. The *P* value of 0.05 is indicated by a horizontal dotted line. Proteins enriched in SKR-2 immunoprecipitates are found in the top right corner of the plot. F-box proteins (orange), SC proteins (green), CUL-1 (brown), SKR-1/2 (magenta), proteasome subunits (cyan), and other proteins (black) are highlighted and listed on the right. (**D**) SMLM localizations within the three boxed regions in fig. S2 (D and E) were straightened, aligned, and rendered to create averaged frontal (*xy*) and cross-sectional (*xz*) views. Scale bars, 100 nm. (**E**) Histogram counts (2-nm-wide bins) of straightened and aligned SMLM localizations along the *x* and *z* axes fitted with Gaussian distributions (black dashed lines). The respective SDs (σ) and peak-to-peak distance of HIM-3 (*d*) are indicated in the plot.

mass spectrometry (Fig. 1B and table S1). As expected, components of the SCF complex that directly bind Skp1, such as CUL-1 and germline-enriched F-box proteins (*34, 35*), and subunits of the 20*S* proteasome were specifically purified with SKR-2 (Fig. 1C). Interestingly, all six previously known SC (SYP-1 to SYP-6) proteins were also purified with SKR-2 and were among the most abundant proteins in the SKR-2 immunoprecipitates, supporting the conclusion that they associate with the SC in *C. elegans*.

SKR-1 and SKR-2 localize to the central region of the SC

We next inserted a hemagglutinin (HA) tag at the N terminus of SKR-1 using CRISPR to determine its localization (fig. S1).

Immunofluorescence revealed that HA::SKR-1 appears as bright puncta during early meiotic prophase, which colocalize with SC protein aggregates known as polycomplexes (arrows in fig. S2A). SKR-1 was then found along the SC in pachytene and dispersed into the nucleoplasm when the SC disassembles in diplotene, while still enriched on the SC "short arm" and in the nucleolus (fig. S2B). We also visualized both SKR-1 and SKR-2 relative to axis proteins, Him-Three Paralog (HTP-3) or High Incidence of Males (HIM-3), using three-dimensional (3D) single-molecule localization microscopy (SMLM) (*9, 36*). The HA tag on the N terminus of SKR-1 and the 3×Flag tag on the C terminus of SKR-2 are positioned at the center of the SC between the two chromosome axes (Fig. 1, D and E, and fig. S2, C to E). Both epitopes were confined to a narrow *z* plane in the cross-sectional view, indicating that SKR-1 and SKR-2 localize at the central region of the *C. elegans* SC.

SKR-1 and SKR-2 are essential for SC assembly

To determine the role of SKR-1 and SKR-2 during meiotic prophase, we first generated a null allele *skr-2(kim66),* which harbors a 50–base pair (bp) deletion immediately after the start codon, resulting in a premature stop after five amino acids (Fig. 2A). *skr-2(kim66)* animals were indistinguishable from the wild-type, displaying normal brood sizes and fertilized egg viability (fig. S1C). This contrasts with the previously characterized *skr-2(ok1938)* allele, which removes not only the second half of its coding sequence and but also a promoter region upstream of *skr-1* that reduces the expression of *skr-1* by ~40% (*37*). *skr-2(ok1938)* mutants laid only 12 eggs on average (compared to 317 in wild-type animals), none of which survived (fig. S1C). *C. elegans* has six pairs of chromosomes, and six 4′,6-diamidino-2-phenylindole (DAPI)–staining bodies representing the six bivalents were observed in diakinesis oocytes of wild-type and *skr-2(kim66)* animals (Fig. 2, B and C). In contrast, 11 to 12 univalents were consistently detected in the few oocytes of *skr-2(ok1938)* mutants that were able to exit pachytene, indicating a failure in crossover formation. Thus, while SKR-2 is dispensable, SKR-1 and SKR-2 together contribute to crossover formation.

As expected, on the basis of the egg viability data, *skr-2(kim66)* animals displayed normal SC assembly (Fig. 2D and fig. S3A). In contrast, *skr-2(ok1938)* animals showed a lack of SYP-5 signal in most pachytene nuclei, and partial SC stretches formed only in late pachytene (Fig. 2D and fig. S3B). Because of these severe synapsis defects, the leptotene/zygotene stage, marked by the crescent-shaped nuclear morphology, was greatly extended in *skr-2(ok1938)* animals. We attempted to generate a mutant that deletes both *skr-1* and *skr-2*.

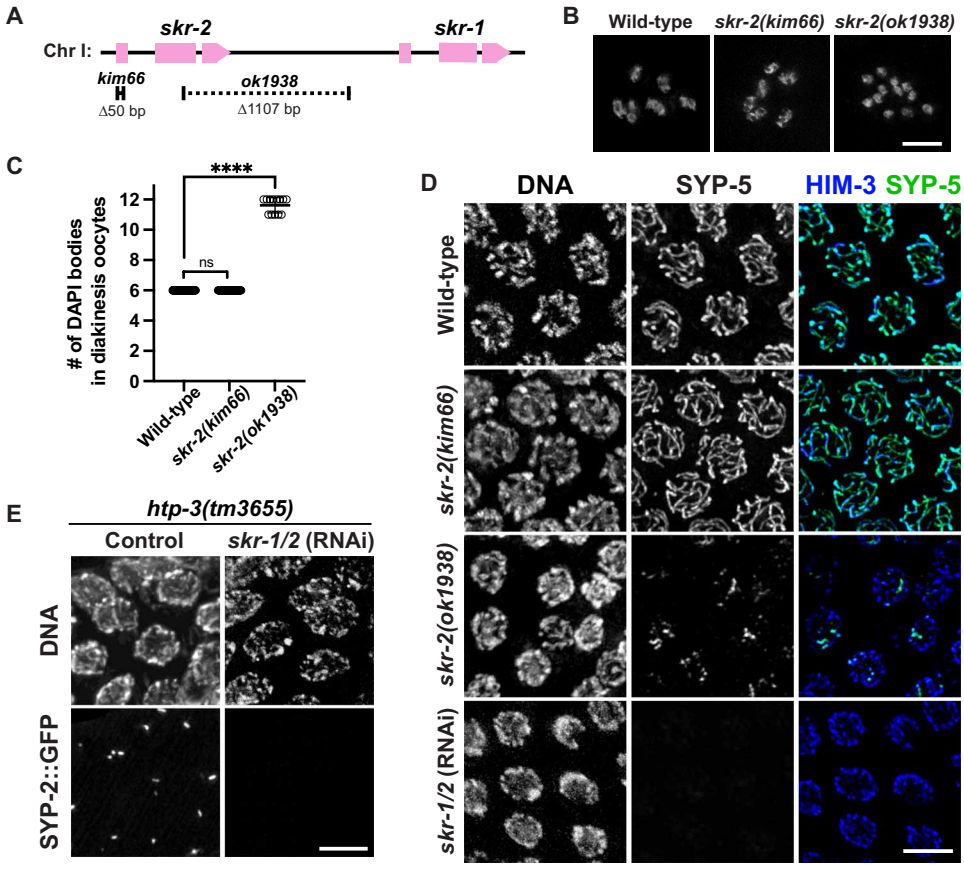

Fig. 2. SKR-1 and SKR-2 are required for SC assembly. (**A**) Schematic showing the *skr* alleles used in this study. (**B**) DAPI-stained oocyte nuclei at diakinesis from indicated genotypes. Scale bar, 3 μm. (**C**) Graph showing the number of DAPI bodies in diakinesis oocytes. The means ± SD are shown. ns, not significant ($P > 0.9999$); ****$P < 0.0001$ by Mann-Whitney *U* test. The numbers of oocytes scored are 30, 29, and 13 for wild-type, *skr-2(kim66)*, and *skr-2(ok1938)*, respectively. (**D**) Immunofluorescence images of pachytene nuclei from the indicated genotypes showing DNA, SYP-5 (green), and HIM-3 (blue) staining. Scale bar, 5 μm. (**E**) *htp-3(tm3655)* animals expressing SYP-2::GFP were treated with control (feeding) and *skr-1/2* RNAi (microinjection), dissected, and stained for DNA and GFP. Scale bar, 5 μm.

However, we were not able to recover homozygous animals due to their essential function during embryo development. Thus, we turned to RNA interference (RNAi) to knock down both *skr-1* and *skr-2* in adult animals and assessed the impact on SC assembly during meiosis. *skr-1/2* RNAi by feeding resulted in strong synapsis defects albeit to varying degrees (Fig. 2D and fig. S3C). To achieve a more penetrant knockdown, we microinjected *skr-1* double-stranded RNA (dsRNA) (1 to 2 μg/μl) into both gonads of L4 larvae and monitored SC morphology using a worm strain expressing SYP-2::GFP (green fluorescent protein). Because *skr-1* and *skr-2* share 83% nucleotide sequence identity, *skr-1* RNAi is expected to also reduce *skr-2* expression. By 2 to 3 days after injection, 22 of 24 injected hermaphrodites displayed a complete loss of SYP-2::GFP signal in the germline. SC polycomplexes were also eliminated when *skr-1* dsRNA was injected into animals lacking an axis component HTP-3 (Fig. 2E). Thus, we concluded that SKR-1 and SKR-2 are required for SC assembly.

CUL-1 does not localize to the SC and is dispensable for synapsis

To assess whether the role of SKR-1/2 in synapsis requires the function of the SCF ubiquitin ligase, we tagged its core scaffolding subunit, CUL-1, with the small epitope Ollas at the C terminus (fig. S1C) and characterized its localization. Although CUL-1 was expressed throughout the germline, it did not show any enrichment on meiotic chromosomes (fig. S4, A and B). Furthermore, CUL-1 was not found in short SYP stretches in *him-3* mutants (fig. S4B), demonstrating that CUL-1 does not associate with the SC. Worms homozygous for a *cul-1* deletion arrest at larval stages due to its role in the cell cycle (*38*). Thus, we used RNAi to knock down *cul-1* expression in later development. An immunoblot showed that >90% of CUL-1 was depleted by RNAi (fig. S5A), which was sufficient to cause a delay in the degradation of PPM-1.D by SCF^{PROM-1} (fig. S5, B and C) as previously reported (*26*, *27*). However, SC assembly occurred normally in *cul-1* RNAi-treated animals (fig. S5D), and knockdown of *cul-1* did not affect SC polycomplexes in *htp-3* mutants (fig. S5E). Thus, CUL-1 appears to be dispensable for synapsis, suggesting that SKR-1 and SKR-2 promote SC assembly independent of their canonical function in the SCF complex.

SKR-1 dimerizes through a conserved hydrophobic interface

Biochemical analyses of recombinant Skp1 from guinea pigs and *Dictyostelium* have revealed that it forms a homodimer at higher concentrations (*39*–*41*). Given the higher-order structure of the SC, we hypothesized that SKR proteins might also dimerize within the SC during *C. elegans* meiosis. This is supported by the detection of peptides unique to SKR-1 in our SKR-2 immunoprecipitates (Fig. 1C), suggesting that SKR-1 and SKR-2 may form a heterodimer in vivo. To determine the oligomeric state of SKR proteins, we expressed and purified 6×His-tagged SKR-1 (21 kDa) from *E. coli* (Fig. 3A) and measured its absolute molar mass using size exclusion chromatography and multiangle light scattering (SEC-MALS). Recombinant SKR-1 was eluted as a single peak with a molecular weight of 40.5 ± 0.9 kDa ($n = 3$), demonstrating that SKR-1 indeed exists as a dimer in solution (Fig. 3B).

The dimer interface of Skp1 is conserved throughout evolution and primarily composed of a hydrophobic surface that overlaps with the core binding site for F-box domain proteins (*34, 39*). An AlphaFold (*42, 43*) model of the truncated SKR-1 dimer (amino acids 1 to 83, GGSG, and 96 to 143) (fig. S6A) superimposes well onto the nuclear magnetic resonance (NMR) structure of the truncated *Dictyostelium* Skp1 dimer (Fig. 3C) (*39*). The conserved phenylalanine (F115) at the SKR-1 dimer interface overlays with F97 in *Dictyostelium* Skp1, whose substitution to glutamic acid was shown to disrupt Skp1 dimerization without affecting the binding to F-box proteins (*39*). Consistent with this, the F115E mutant of *C. elegans* SKR-1 was monomeric in solution, as indicated by its measured molar mass of 21.0 ± 1.1 kDa ($n = 3$) by SEC-MALS (Fig. 3, A and B).

The dimer interface of SKR proteins is essential for SC loading and assembly

To investigate the significance of SKR dimerization in SC assembly, we introduced the F115E mutation in the *ha::skr-1* worm strain using CRISPR. The *ha::skr-1*^{F115E} strain exhibited a normal brood size and produced mostly viable progeny (fig. S7, A and B). However, HA::SKR-1^{F115E} failed to localize along the SC (fig. S7C), although it is expressed, albeit at a reduced level compared to the wild-type protein (fig. S7D). When the *skr-1*^{F115E} mutation was introduced into the *skr-2(kim66)* background, a substantial reduction in egg viability was observed, with only 2% of eggs surviving and 19% of the progeny being male (fig. S7B), which arises from X-chromosome nondisjunction during meiosis (*44*). Notably, SC assembly completely failed in the double *skr-1*^{F115E} *skr-2(kim66)* mutant, resulting in an extension of the transition zone corresponding to a prolonged leptotene/zygotene stage (Fig. 4, A and B, and fig. S3D). However, unlike the phenotypes observed in *skr-2(ok1938)* mutants or after *skr-1/2* RNAi (*26*, *27*), there was no delay in the degradation of PPM-1.D or the onset of meiotic prophase in these animals (fig. S8, A and B), indicating that SCF activity was intact. In addition, meiotic cells successfully progressed through pachytene, and oocytes were produced (Fig. 4A). Thus, the major cell cycle transitions controlled by SCF occurred normally in the germline of *skr-1*^{F115E} *skr-2(kim66)* mutants. However, oocytes in these animals consistently displayed 10 to 12 DAPI-staining bodies (Fig. 4, C and D), indicating an inability to form crossovers due to synapsis failure. These phenotypes are indistinguishable from those lacking other SC proteins (*9*–*14*), demonstrating that the dimer interface of SKR proteins is essential for SC assembly.

SKR-2 repurposes its SCF-forming interfaces to interact with the SC proteins

We next asked whether SKR proteins use the other SCF-forming interfaces to incorporate into the SC. The Skp1-Cul1 interaction is mediated through the BR-C, ttk and bab (BTB)/Pox virus and Zinc finger (POZ) fold of Skp1, and mutating two residues in the H5 helix of human Skp1 has been shown to abolish its binding to Cul1 (*35*). Thus, we mutated the corresponding residues in SKR-1 (N122K and Y123K) and SKR-2 (N120K and Y121K) in *C. elegans* to examine the importance of this interface in SC loading. While an *skr-2::3×flag* strain harboring the N120K and Y121K mutations was fully viable (fig. S1C), animals homozygous for the equivalent mutations in *skr-1* could not be recovered, reflecting its essential role in embryo development (*33*). Interestingly, SKR-$2^{N120K,Y121K}$ failed to localize along the SC, although it was clearly expressed (fig. S9, A and B). SEC-MALS analyses revealed that recombinant SKR-$1^{N122K,Y123K}$ is monomeric in solution with an average molecular weight of 21.6 ± 2.6 kDa ($n = 3$) (fig. S9C), explaining the inability of SKR-$2^{N120K,Y121K}$ to load onto the SC. An AlphaFold (*42, 43*)

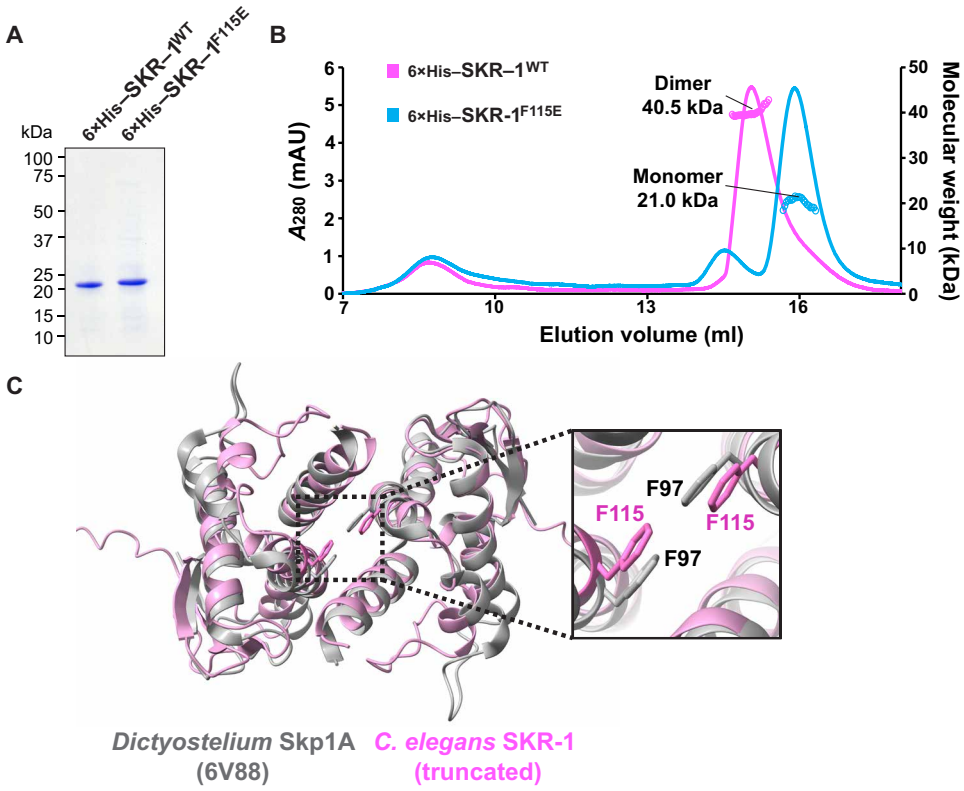

Fig. 3. Recombinant SKR exists as a dimer in solution. (**A**) An SDS-PAGE gel showing the purification of recombinant 6×His-SKR-1^{WT} and 6×His-SKR-1^{F115E}. (**B**) SEC-MALS traces of 6×His-SKR-1^{WT} (magenta) and 6×His-SKR-1^{F115E} (light blue). Absorbance at 280 nm (A_{280}) is shown on the left axis, and the measured molecular weight is shown on the right axis. mAU, milli–arbitrary units. (**C**) An AlphaFold model of a truncated *C. elegans* SKR-1 (amino acids 1 to 83, GGSG, and 96 to 143; magenta) superimposed onto the NMR structure of a truncated *D. discoideum* Skp1A dimer (gray; Protein Data Bank 6V88) (*39*). The inset shows the conserved phenylalanine (F97 in *Dictyostelium* Skp1A and F115 in *C. elegans* SKR-1) at the dimerization interface.

model of the full-length SKR-1 dimer (fig. S6B) shows that the CUL-1–binding interface of SKR proteins is within its dimer interface (fig. S9, D and E), suggesting that SKR dimerization is likely to interfere with CUL-1 binding.

Skp1 interacts with the F-box protein through a bipartite interface that involves the variable C-terminal helices of Skp1 (*34*). To investigate the role of these helices in SC loading, we mutated two conserved residues in SKR-2 located at the end of H7 and H8 helices (I153A and W171A), similar to mutations that disrupt Skp1's cell cycle function in budding yeast (*34, 45*). Importantly, these helices reside outside of the Skp1 dimer interface (Fig. 5A), and recombinant SKR-1 harboring the equivalent mutations (I155A and W173A) still formed a dimer in our SEC-MALS analyses (39.7 ± 1.3 kDa; $n = 3$) (Fig. 5B). Because of the redundancy between *skr-1* and *skr-2*, animals harboring the *skr-2*^{I153A,W171A} mutations formed the SC and supported normal meiotic progression (fig. S1C). However, the SKR-2^{I153A,W171A} protein failed to localize along the SC (Fig. 5, C and D), suggesting that SKR proteins require the C-terminal helices to associate with SC proteins. To test this, we immunoprecipitated 3×Flag-tagged SKR-2^{I153A,W171A} from isolated germline nuclei and analyzed its interacting proteins using mass spectrometry (Fig. 5E). Indeed, SKR-2$^{I153A, W171A}$ failed to pull down the SYP proteins and most F-box proteins (Fig. 5F and table S2), confirming that SKR proteins repurpose their F-box protein–binding C-terminal helices to interact with meiosis-specific SC proteins.

SKR-1 forms a soluble complex with previously known SC components in vitro

To establish SKR proteins as bona fide subunits of the SC, we turned to in vitro reconstitution and expressed SKR-1 along with five SYP proteins in bacteria using a polycistronic plasmid. Because of the redundancy between SKR-1 and SKR-2 and between SYP-5 and SYP-6 (*9*, *10*), SKR-2 and SYP-6 were omitted. Our previous attempts to coexpress and purify the SYP proteins from bacteria were unsuccessful because of their insolubility. However, adding *skr-1* to the polycistronic expression plasmid was sufficient to solubilize all SYP proteins, enabling the purification of 6×His-SYP-3, along with untagged SYP-1, SYP-2, SYP-4, SYP-5, and SKR-1 (Fig. 6A), which we confirmed by mass spectrometry (Fig. 6B). Interestingly, 6×His–SYP-3–containing protein complexes eluted from a cation exchange column as two separate peaks (Fig. 6A). Subsequent SEC-MALS analyses revealed that 6×His-SYP-3 formed two distinct complexes: a ~1-MDa complex consisting of SYP-3, SYP-4, and SKR-1 (peak 1) (Fig. 6C) and a ~1-MDa complex containing all five SYPs and SKR-1 (peak 2) (Fig. 6D). As all six SC proteins are dependent on each other for chromosomal loading (*9*–*14*), the SYP-3/SYP-4/SKR-1 complex is likely an in vitro artifact that represents the stable association between SKR-1, SYP-3, and SYP-4. The intensities of Flamingo-stained bands suggest an equal stoichiometry of all constituents in both complexes (Fig. 6, C and D), and the measured molecular weights are consistent with stoichiometries of 8 to 10 each for the

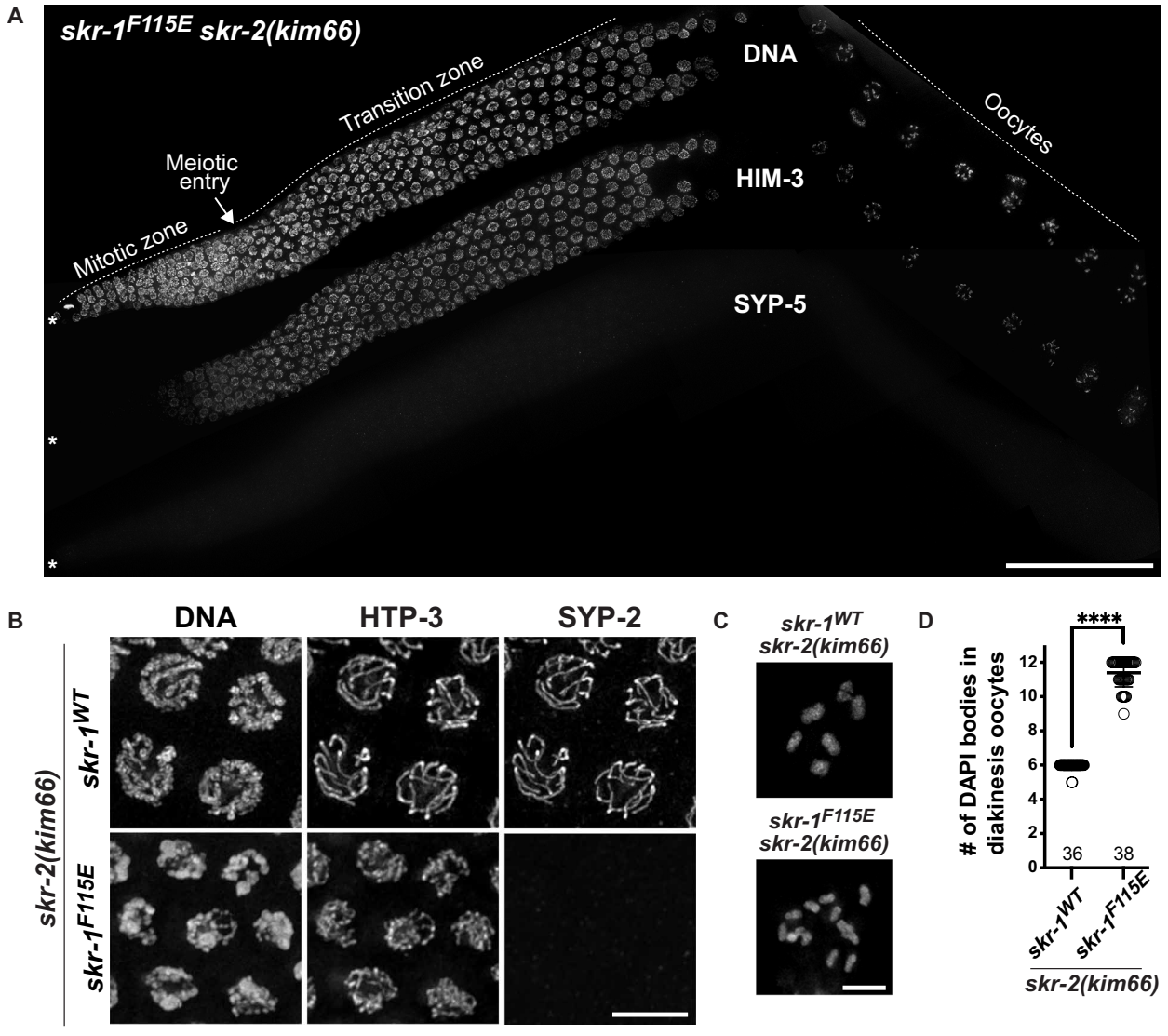

Fig. 4. Dimerization of SKR proteins is essential for synapsis. (**A**) Composite immunofluorescence images of a full-length gonad dissected from an *skr-1*^{F115E} *skr-2(kim66)* animal are shown for DNA, HIM-3, and SYP-5 staining. Asterisk (*) indicates the distal tip. Scale bar, 50 μm. (**B**) Immunofluorescence images of pachytene nuclei from *skr-2(kim66)* and *skr-1*^{F115E} *skr-2(kim66)* animals showing DNA, HTP-3, and SYP-2 staining. Scale bar, 5 μm. (**C**) DAPI-stained oocyte nuclei at diakinesis from *skr-2(kim66)* and *skr-1*^{F115E} *skr-2(kim66)* animals. Scale bar, 3 μm. (**D**) Graph showing the number of DAPI bodies in diakinesis nuclei from indicated genotypes. The numbers of nuclei scored are shown below. The means ± SD is shown; ****$P < 0.0001$ by the Mann-Whitney *U* test.

SYP-3/SYP-4/SKR-1 complex (914 to 1143 kDa expected) and 4:4:4:4:4:4 for the six-protein complex (all five SYPs and SKR-1; 1029 kDa expected). These results establish SKR-1/2 as key missing components of the SC and suggest that a core set of SC subunits has now been identified in *C. elegans*.

DISCUSSION

Our work has uncovered a moonlighting function of Skp1 proteins as structural components of the SC in *C. elegans*. SC assembly requires the dimerization of SKR-1/2 through an interface that overlaps with the binding sites for Cul1 and F-box proteins. Therefore, the dimerization of SKR-1/2 prevents the formation of the SCF complex, providing the molecular basis for their dual function (Fig. 6E).

During the mitosis-to-meiosis transition, SCF^{PROM-1} complexes down-regulate proteins involved in the mitotic cell cycle (*26*–*28*). Since substrate availability enhances the stability of its cognate SCF complex (*46, 47*), degradation of SCF^{PROM-1} substrates might promote the rapid exchange of PROM-1–SKR-1/2 modules from CUL-1, leading to the eventual disassembly of SCF^{PROM-1} complexes. The dissociation constant (K_D) for Skp1 dimerization ranges from 1 to 2.5 μM (*39, 40*), while Skp1's binding affinity for F-box proteins is approximately 100-fold higher (*48*). Thus, the dimerization of SKR-1/2 is expected when the local concentration of SKR-1/2 rises above the micromolar concentration range. Although the endogenous

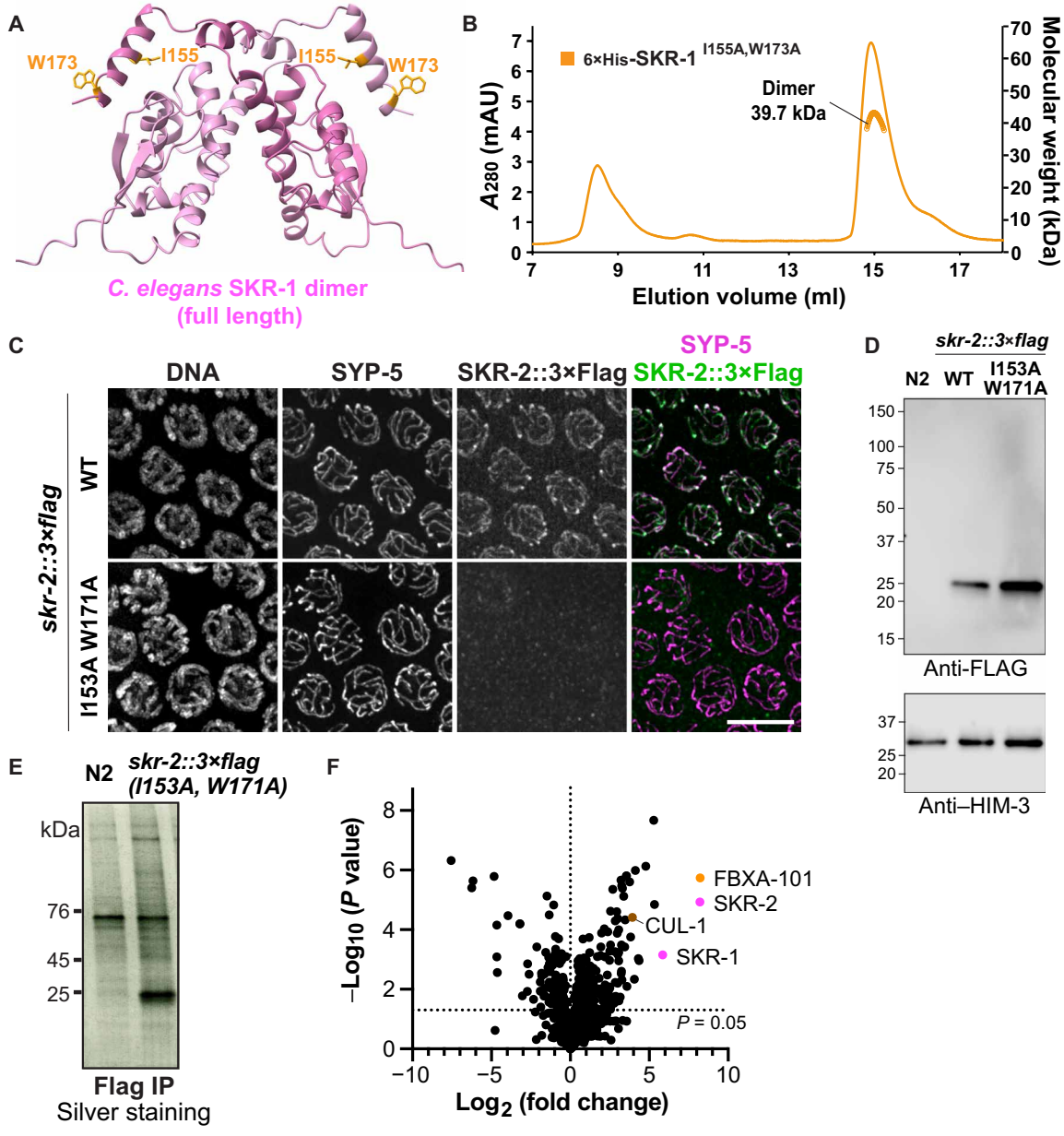

Fig. 5. SKR-2 interacts with the SYP proteins via the SCF-forming interfaces. (**A**) An AlphaFold model of the *C. elegans* SKR-1 dimer with mutated residues highlighted. (**B**) An SEC-MALS trace of 6×His-SKR-1^{I155A,W173A}. The absorbance at 280 nm is shown on the left axis, and the measured molecular weight is shown on the right axis. (**C**) Immunofluorescence images of pachytene nuclei from *skr-2::3×flag* worm strains harboring wild-type and the I153A and W171A mutation. DNA, SYP-5, and SKR-2::3×Flag staining are shown. Scale bar, 5 μm. (**D**) Immunoblots of worm lysates from the indicated genotypes probed against the 3×FLAG tag fused to the C terminus of SKR-2. N2 was used as a negative control, and HIM-3 was used as a loading control. (**E**) A silver-stained SDS-PAGE gel showing purified SKR-2^{I153A,W171A}-containing protein complexes using anti-Flag beads from worm lysates. N2 was used as a control. (**F**) A volcano plot showing proteins enriched in SKR-2::3×flag^{I153A,W171A} immunoprecipitates over N2 control. Normalized weighted spectra were transformed to logarithmic values (base 2) and analyzed by multiple unpaired *t* tests. The logarithm of fold change (base 2) is plotted on the *x* axis, and the negative logarithm of the *P* value (base 10) is plotted on the *y* axis. The *P* value of 0.05 is indicated by a horizontal dotted line.

concentration of SKR-1/2 is unknown in the *C. elegans* germline, the concentration of Skp1 in mammalian cells was measured to be 1 to 2 μM (*46*), which can permit Skp1 dimerization. Condensation of the SC materials into phase-separated polycomplexes may increase the local concentrations of SKR-1/2 and the SYP proteins (*49*), enabling the dimerization of SKR-1/2 and subsequent SC polymerization (Fig. 6E). We also speculate that signals produced during meiotic entry might weaken the interaction between SKR-1/2 and F-box proteins and help exclude F-box proteins from phase-separated SC compartments. Intriguingly, two conserved residues in the C-terminal helices of SKR-1 have been mapped to be phosphorylated in vivo, and phosphorylation at the equivalent residue in budding yeast Skp1 has been shown to impair its interaction with an F-box protein, Met30 (*50*). Therefore, we envision a

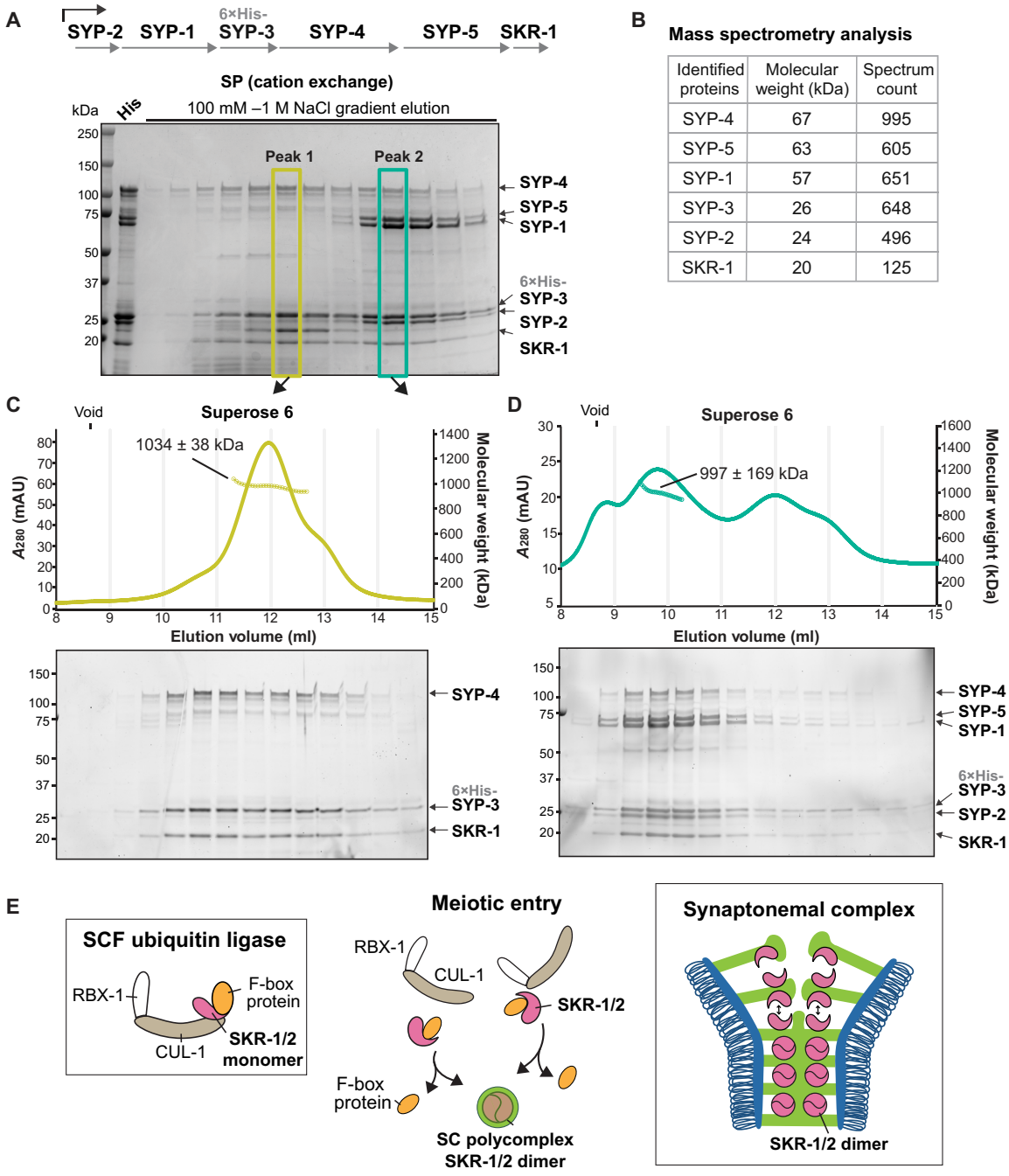

Identified proteins	Molecular weight (kDa)	Spectrum count
SYP-4	67	995
SYP-5	63	605
SYP-1	57	651
SYP-3	26	648
SYP-2	24	496
SKR-1	20	125

Fig. 6. In vitro reconstitution establishes SKR-1/2 as SC subunits. (**A**) Schematic of the polycistronic plasmid used to coexpress SKR-1 and the SYP proteins (top) and a Coomassie-stained SDS-PAGE gel of the SYP/SKR-1 complexes purified using a 6×His tag on SYP-3 (His) and cation exchange chromatography (SP). Two peak fractions eluted from the SP column are highlighted. (**B**) Table showing the results from mass spectrometry analysis. (**C** and **D**) SEC-MALS traces and Flamingo-stained SDS-PAGE gels of the SYP-3/SYP-4/SKR-1 complex (peak 1; 1034 ± 38 kDa; $n = 4$) and the complex that contains all six proteins (peak 2; 997 ± 169 kDa; $n = 3$). The absorbance at 280 nm is shown on the left axis, and the measured molecular weight is shown on the right axis. The void volume is indicated on the top. (**E**) The model for the dual functions of SKR-1/2 within the SCF ubiquitin ligase complex versus the SC.

scenario in which meiotic kinases promote the dimerization of SKR-1/2 and condensation of SC proteins, thereby coupling SC assembly with the onset of meiotic differentiation.

The function of SKR proteins within the SC is analogous to that of Skp1 at the budding yeast centromere. In budding yeast, Skp1 forms the centromeric DNA-binding factor 3 (CBF3) complex with three kinetochore proteins, Chromosome transmission fidelity 13 (Ctf13), Nuclear division cycle 10 (Ndc10), and Chromosomal gene 3 (Cep3), that are present only in fungi with point centromeres (*51*) to direct the assembly of centromeric nucleosomes (*45*, *52*). Skp1

uses the Cul1-binding interface to interact with Cep3 (*53, 54*), which prevents it from forming SCF complexes once incorporated into the CBF3 complex. Thus, Skp1 proteins have been co-opted to interact with different sets of rapidly evolving proteins outside of the context of the SCF ubiquitin ligase, serving as structural components of chromosome scaffolds that are essential for both mitosis and meiosis. The formation of the CBF3 complex is known to substantially enhance the stability of Ctf13, an F-box protein, which is otherwise susceptible to degradation through SCF-mediated polyubiquitination (*55, 56*). It is possible that, similar to Ctf13, SYP proteins are protected from degradation once incorporated into the SC, although it is unknown whether SYP proteins are targeted by the SCF complex for proteolysis. Regardless, the structural function of SKR-1/2 within the SC has implications for its disassembly. As the SC starts to disassemble at the end of pachytene, germline-enriched F-box proteins could potentially function as a "molecular sponge" by sequestering SKR-1/2, thereby accelerating desynapsis. Given the high affinity between SKR-1/2 and F-box proteins, the mere presence of F-box proteins will be sufficient to outcompete for SKR-1/2 binding and may not require the SCF activity.

While proteins that make up the SC are known for their rapid evolution and prevalent coiled-coil domains (*7*, *8*), Skp1 proteins do not share these characteristics and exhibit a high degree of sequence conservation across eukaryotes (*57*). It has yet to be determined how widespread the structural function of Skp1 is conserved beyond *C. elegans* and what their evolutionary trajectory entails. Nevertheless, our study has uncovered a fascinating example of meiotic regulation, wherein a highly conserved cell cycle regulator has acquired a unique function as a component of the SC. Future work identifying the regulatory mechanisms that control the switch between their dual roles and delineating the protein-protein interactions between SKR-1/2 and the SYP proteins will provide crucial insights into the organizing principles of the SC and how its assembly and disassembly are coupled to cell cycle progression.

MATERIALS AND METHODS

C. elegans strains and CRISPR-mediated genome editing

We adhere to the National Institutes of Health Guide for the Care and Use of Laboratory Animals. All strains used in this study were maintained on Nematode growth medium (NGM) plates seeded with OP50-1 bacteria under standard conditions (*58*). All experiments were performed at 20°C. All *C. elegans* strains were derived from Bristol N2 background. Some strains were provided by the *Caenorhabditis* Genetics Center, which is funded by the National Institutes of Health Office of Research Infrastructure Programs (P40 OD010440). Table S5 summarizes all mutations and strains used in this study.

To generate strains expressing SKR-1::3×Flag, HA::SKR-1, SKR-2::3×Flag and a null allele *(kim66)* of *skr-2*, N2 or worms expressing GFP::CrossOver Site Associated (COSA)–1 were injected with Cas9 (0.25 μg/μl; 2 nmol) complexed with 10 μM transactivating CRISPR RNA/CRISPR RNA oligos [Integrated DNA Technologies (IDT)], pRF4::rol-6(su1006) (40 ng/μl), and an single-stranded DNA oligo (200 ng/μl; IDT) with 35-bp homology arms on both sides as a repair template (table S4). F1 progeny were lysed and genotyped by polymerase chain reaction (PCR) to detect successful edits. The correct insertion was validated by Sanger sequencing.

To generate the F115E mutation of *skr-1*(*kim74*) and N120K Y121K *(kim76)* or I153A W173A mutations (*kim78)* of *skr-2*, YKM616 (*ha::skr-1*) or YKM219 (*skr-2::3×flag*) worms were injected respectively with 16 μM Cas9 complexed with 16 μM transactivating CRISPR RNA/CRISPR RNA oligos (IDT), pCFJ104 (5 ng/μl), pCFJ90 (2.5 ng/μl), and a single-stranded DNA oligo (100 ng/μl; IDT) as a repair template. F1 progeny were lysed and genotyped by PCR to detect successful edits. The correct insertion was validated by Sanger sequencing. The worm strain expressing SYP-2::TEV::GFP (YKM853) was made by InVivo Biosystems using CRISPR.

Immunoprecipitation of SKR-2-containing protein complexes

N2, YKM219 (*skr-2::3×flag*), and YKM942 (*skr-2::3×flag*^{I153A,W171A}) worms were grown in liquid culture in a developmentally synchronous manner at 20°C. Young adult worms were harvested by sucrose flotation, frozen in liquid nitrogen, and ground into a frozen powder using a Retsch Mixer Mill. The frozen powder was then resuspended in 2× volume of nuclear purification buffer [50 mM Hepes (pH 7.5), 40 mM NaCl, 90 mM KCl, 2 mM EDTA, 0.5 mM EGTA, 0.2 mM dithiothreitol (DTT), 0.5 mM phenylmethylsulfonyl fluoride, 5 mM spermidine, 0.247 mM spermine, and cOmplete protease inhibitor cocktail (Sigma-Aldrich, 11697498001)] and was passed through two 40-μm, two 30-μm, and two 20-μm cell strainers (pluriSelect, 43-50040-50, 43-50030-50, and 43-50020-50) to isolate germline nuclei as previously described (*59*). The nuclei were collected by centrifugation at 3100 rpm for 6 min at 4°C, and the pelleted nuclei were resuspended in 2× the volume of lysis buffer [50 mM tris-HCl (pH 8.0), 150 mM NaCl, 5 mM $MgCl_2$, 1 mM EGTA, 0.1% NP-40, 10% glycerol, and cOmplete protease inhibitor cocktail]. The isolated nuclei were transferred to a new tube and nutated for 10 min at 4°C for lysis to complete. The nuclear lysates were cleared by centrifugation at 4000 rpm for 10 min, and the supernatant was incubated with anti-FLAG M2 magnetic beads (Sigma-Aldrich, M8823) for 10 to 20 min at 4°C to prevent the exchange of SCF subunits after cell lysis (*46*). The beads were then washed three times in the lysis buffer supplemented with 300 mM NaCl, and SKR-2–containing protein complexes were eluted overnight in 100 μl of the lysis buffer containing 3×Flag peptide (2 mg/ml; Sigma-Aldrich, F4799). Eluted protein samples were digested with trypsin and analyzed by MudPIT in the Mass Spectrometry and Proteomics Facility at Johns Hopkins School of Medicine.

Flag immunoprecipitation was performed in three biological replicates. Spectrum counts were normalized in Scaffold 5 (Proteome Software) by multiplying the average number of spectra across all biological samples over the total number of spectra in each sample. Normalized spectra were converted to logarithms (base 2) and were analyzed by multiple unpaired *t* tests (GraphPad Prism 9) to identify proteins enriched in SKR-2::3×Flag immunoprecipitates.

Egg count

L4 hermaphrodites were picked onto individual NGM plates and transferred to new plates every 12 hours for a total of 4 to 5 days. Eggs and hatched L1s were counted immediately after the transfer, and surviving progeny and males on each plate were counted when F_1 reached adulthood.

RNA interference

The study used two methods to carry out RNAi, feeding, and microinjection. For feeding RNAi, N2, YKM874 [*htp-3(tm3655); syp-2::tev::gfp*], YKM218 (*cul-1::Ollas*), or YKM183 (*ppm-1.D::ha*)

hermaphrodites were fed with the *Escherichia coli* strain HT115 (DE3) carrying an Ahringer RNAi library clone of *skr-1* (*60*), a Vidal RNAi library clone of *cul-1* (*61*), or the empty L4440 vector. Concentrated bacterial cultures were seeded onto RNAi plates [NGM, 1 mM isopropyl-β-D-thiogalactopyranoside, and carbenicillin (100 μg/ml)], left for 1 hour in the laminar fume hood to dry, and incubated for 3 days at 37°C to induce expression of dsRNA. L1 hermaphrodites were picked onto seeded RNAi plates and left for 3 to 4 days at 20°C before dissection for immunofluorescence. *skr-1* RNAi by feeding resulted in variable phenotypes with incomplete penetrance.

For *skr-1* RNAi by microinjection, a coding sequence within exon 2 was amplified by PCR from the genomic DNA of N2 worms using primers with the T7 promoter sequence attached to the 5′ ends (forward, taatacgactcactataggAAACACTATCAACACTCTCC; reverse, taatacgactcactataggATGAGCTCGAAAAGGGTTCC). Sense and antisense single-stranded RNAs were synthesized in vitro using the MEGAscript T7 Transcription Kit (Thermo Fisher Scientific) and annealed by incubation at 70°C for 10 min and gradual cooling to 20°C. Upon treatment with TURBO deoxyribonuclease (Invitrogen) and ribonuclease A (Thermo Fisher Scientific), dsRNA was purified using phenol-chloroform extraction and verified by gel electrophoresis. dsRNA (1 to 1.8 μg/μl) was injected into both gonad arms of YKM853 (*syp-2::tev::gfp)* animals at the L4 stage. The knockdown efficiency of RNAi was optimized by monitoring the SYP-2::GFP signal.

Immunofluorescence

Adult hermaphrodite germlines were dissected 24 hours after L4 larval stage in egg buffer [25 mM Hepes (pH 7.4), 118 mM NaCl, 48 mM KCl, 2 mM EDTA, 5 mM EGTA, 0.1% Tween 20, and 15 mM NaN_3] except for *skr-1* RNAi-microinjected animals, which were dissected 2 to 3 days after L4 larval stage. Dissected germlines were fixed in 4 to 10% formaldehyde before freezing in liquid nitrogen, freeze-cracked, and fixed again in −20°C methanol for 1 min. Samples were then rehydrated with PBST [13.7 mM NaCl, 0.27 mM KCl, 1 mM Na_2HPO_4, 0.18 mM KH_2PO_4 (pH 7.4), and 0.1% Tween 20] and blocked with Roche blocking reagent (Sigma-Aldrich, 11096176001) for 1 hour at room temperature. Incubation with primary antibodies was performed overnight at 4°C at the following concentrations: FLAG (mouse; 1:1000; Sigma-Aldrich, F1804), HA (mouse; 1:500; Invitrogen, 2-2.2.14), SYP-2 (rabbit; 1:500) (*9*), SYP-5 (rabbit; 1:500) (*9*), HIM-3 (chicken; 1:500) (*9*), HTP-3 (guinea pig; 1:500) (*9*), GFP booster Alexa Fluor 488 (1:200; Proteintech, gb2AF488), and Ollas (rat; 1:500; Invitrogen, MA5-16125). Slides were washed with PBST and incubated with secondary antibodies for 30 min at room temperature at a 1:200 dilution (Sigma-Aldrich or Invitrogen Alexa Fluor 488, Alexa Fluor 555, or Alexa Fluor 647). Slides were washed again with PBST, stained with DAPI, and mounted in ProLong Gold (Invitrogen, P36930). Slides were cured for 1 day before imaging.

Most images were captured with a DeltaVision Elite system (Cytiva) equipped with a 100× oil immersion, 1.4 numerical aperture (NA) objective, and an scientific complementary metal-oxide semiconductor camera [Pioneering in Cameras and Optoelectronics (PCO)]. 3D image stacks were collected at 0.2-μm intervals, processed by iterative deconvolution (enhanced ratio, 20 cycles), and projected using the SoftWoRx package. Composite images were assembled and colored using Adobe Photoshop. Images shown in fig. S5B were captured by a Leica Thunder Imaging System equipped with a 100× oil immersion, 1.4 NA objective, and a Leica K8 camera. 3D image stacks were collected at 0.2-μm intervals and processed by large volume computational clearing using Global Strategy (the feature scale, 341 nm; 92% strength; 30 iterations). Image stacks were projected using the LAS X software, and the projected images were assembled and colored using Adobe Photoshop.

Single-molecule localization microscopy

Sample preparation

Adult worms (24 hours after L4) were dissected and immunostained as described previously (*62*). Dissected and fixed tissue was incubated overnight at 4°C with anti-Flag (mouse; 1:200; Sigma-Aldrich, F1804) or anti-HA (mouse; 1:200; Invitrogen, 2-2.2.14), and anti-HIM-3 (rabbit polyclonal; 1:200 or 1:100; Novus Biologicals, #53470002) or anti-HTP-3 (chicken polyclonal; 1:200) (*63*) primary antibodies. The first incubation was followed by three 5- to 15-min washes with PBST to remove unbound primary antibodies. Samples were subsequently stained with F(ab′)2 fragments conjugated with organic fluorophores: Alexa Fluor 647 (Thermo Fisher Scientific, A37573) anti-mouse immunoglobulin G (IgG) (donkey polyclonal; 1:50; Jackson ImmunoResearch, AB_2340761), and CF680 (Biotium 92139) anti-rabbit IgG (donkey polyclonal; 1:50; Jackson ImmunoResearch, AB_2340586) or anti-chicken IgY (donkey polyclonal; 1:50; Jackson ImmunoResearch, AB_2340347). Working antibody solutions were prepared in 1× Roche blocking buffer (Sigma-Aldrich, 11096176001). Samples were mounted within a custom-built holder filled with 1 ml of imaging buffer [50 mM tris-HCl (pH 8.0), 10 mM NaCl, 10% D-glucose, 35 mM 2-mercaptoethylamine, glucose oxidase (500 μg/ml), and catalase (40 μg/ml)], and sealed with parafilm (*64, 65*).

SMLM imaging

SMLM imaging was performed at room temperature on a custom-built microscope (*66, 67*). Briefly, samples were excited by a Luxx 638-nm laser coming from a LightHub laser combiner (Omicron-Laserage Laserprodukte, Dudenhofen, Germany) and an additional booster laser (Toptica Photonics iBEAM-SMART-640-S, Gräfelfing, Germany). The two lasers were combined by a polarizing beam splitter and coupled into a square multimode fiber (Thorlabs, M103L05, Newton, NJ, USA). An effective homogeneous illumination was achieved through speckle reduction by mechanical agitation of the fiber (*68*). The output of the multimode fiber was first magnified by an achromatic lens and then focused on the sample. A laser cleanup filter (390/482/563/640 HC Quad; AHF, Tübingen, Germany) was introduced in the illumination path to remove fluorescence generated by the fiber (*68, 69*). The emitted light was gathered by a high-NA oil-immersion objective (160×/1.43 NA; Leica, Wetzlar, Germany) and passed through an astigmatic lens ($f = 1000$ mm; Thorlabs) to allow for 3D SMLM image reconstruction. The dual-color acquisition was achieved by ratiometrically splitting the emission light by a 665-nm long-pass dichroic mirror (Chroma, ET665lp) and by filtering the transmitted and reflected photons by a 685/70 (Chroma, ET685/70 m) and a 676/37 (Semrock, FF01-676/37-25) filter, respectively. Both reflected and transmitted emissions were recorded as separate channels at distinct parts of the same electron-multiplying charge-coupled device camera (Photometrics, Evolve512D). During the course of SMLM acquisitions, the focus was stabilized by detecting the total internal reflection of an infrared laser (iBeam Smart, Toptica, Munich, Germany) on the coverslip using a quadrant photodiode that was in a closed feedback loop with the piezo objective positioner (Physik Instrumente) (*70*). A field-programmable gate array (FPGA; Au; Embedded Micro) was used to control the lasers, switch

filters, and stabilize the focus (*71*). The FPGA is controlled by Easier Micro-Manager User interface (EMU) (*72*), a custom-written plugin for Micro-Manager 2.0.0 (*73, 74*). The samples were exposed to the 638-nm illumination at high irradiance of about 13 kW/cm^2 until an appropriate fluorophore blinking rate was achieved. Subsequently, 150,000 to 200,000 frames were acquired with an exposure time of 20 ms and irradiance (20 kW/cm^2) (*68, 69*).

SMLM image reconstruction and postprocessing

All postprocessing of raw data were performed using the SMAP software (Super-resolution Microscopy Analysis Platform; https://github.com/jries/SMAP) (*75*). Single emitters were localized in the acquired SMLM images by the global fitting algorithm *globLoc* (*70*) within the SMAP software using an experimental Point Spread Function (PSF) model and linking all three coordinates of the emitters between the two channels. The experimental astigmatic PSF model and the transformation between the two channels were generated from *z*-stack images of fluorescent beads (TetraSpeck Microspheres, T7279, Thermo Fisher Scientific) that were acquired before each SMLM experiment (*76*). Subsequently, sample drift was corrected by a custom algorithm based on redundant cross-correlation within the SMAP software as described previously (*69*). Furthermore, dim and out-of-focus emitters were rejected by filtering localizations according to their localization precision and their *z* position, respectively. To this end, we have filtered all localizations with *z* positions outside of the −300 to 300 nm range, as well as the localizations with a localization precision above 15 nm in lateral (*xy*) and 30 nm in axial (*z*) direction. Channel assignment of the individual localizations was performed according to their relative brightness in the two channels. The super-resolved image was reconstructed by plotting Gaussians at the fitted positions with a width proportional to their localization precision and assigning the color based on the assigned channel.

Data analysis

To assess the quality of the SMLM images, their Fourier ring correlation (FRC) resolution (*77, 78*) was estimated by the *FRC resolution* plugin from SMAP software (*75*). To create frontal and cross-sectional views of the SMLM localizations (Fig. 1 and fig. S2), midlines of the SC stretches were manually annotated. SMLM localizations around the annotated polyline were straightened, aligned, and rendered to create displayed views using custom MATLAB (R2022a) scripts that can be run from the SMAP software (*75*). *Line profiles* SMAP plugin was used to plot the profiles (histograms with 2-nm bin width) of straightened localizations along the *x* and *z* axes. Generated profiles for each localized SC component (HIM-3 and SKR-2::3×Flag) were fitted by a double or a single-peak Gaussian to describe their distributions within the annotated regions. Histogram counts and the fitted Gaussian distributions were plotted by a custom R (version 4.4.2) script using the *ggplot2* package.

Protein expression and purification

The open reading frame of SKR-1 was synthesized as a gBlock (IDT) and inserted into the pMAL-c6T vector [New England Biolabs (NEB)] to express 6×His–MBP (maltose-binding protein) fused to the N terminus of SKR-1. After confirming that SKR-1 was soluble without MBP, the coding sequence for MBP was removed by Q5 site-directed mutagenesis (NEB) to express 6×His-SKR-1. The F115E, N122K Y123K, and I155A W173A mutations were introduced by Q5 site-directed mutagenesis (NEB) (table S6). To construct a polycistronic vector for expressing SYPs and SKR-1, synthetic gBlocks (IDT) or gene fragments amplified from a *C. elegans* cDNA library were ligated into pET23 (Novagen) via Gibson assembly. Each translation cassette contains the translation enhancer and Shine-Dalgarno sequence upstream of the start codon. Protein expression was induced in Rosetta2(DE3)pLysS cells (Novagen) at 15°C with 0.1 mM isopropyl-β-D-thiogalactopyranoside for 16 hours. Bacterial cell pellets were flash-frozen, resuspended in the lysis buffer (phosphate-buffered saline, 300 mM NaCl, 50 mM imidazole, 0.5 mM EGTA, 2 mM $MgCl_2$, and 1 mM DTT) containing cOmplete protease inhibitor cocktail, and lysed by sonication. After centrifugation at 13,000 rpm (Beckman Coulter, JA-17) for 45 min, the supernatant was loaded to a HisTrap HP column (Cytiva) and washed with binding buffer (phosphate-buffered saline, 300 mM NaCl, 50 mM imidazole, 0.5 mM EGTA, 2 mM $MgCl_2$, and 1 mM DTT). 6×His-SKR-1 proteins and the SYP/SKR-1 complexes were eluted in the binding buffer with 500 mM imidazole. Eluted fractions were pooled and run over a HiTrap SP HP column (Cytiva) to remove contaminating proteins. For the variants of 6×His-SKR-1, the flow-through from the HiTrap SP column was collected and centrifuged to concentrate in an Amicon Ultra-4 centrifugal filter (Sigma-Aldrich, UFC8010). The SYP/SKR-1 complexes bound to the HiTrap SP column were eluted using a 100 mM to 1 M NaCl gradient in 50 mM Hepes (pH 7.5), 0.5 mM EGTA, 5 mM $MgCl_2$, and 1 mM DTT. Two elution peaks from the SP column were further analyzed by SEC-MALS. To validate proteins' identity, proteins eluted from the SP column was digested with trypsin and analyzed by MudPIT in the Mass Spectrometry and Proteomics Facility at Johns Hopkins School of Medicine.

AlphaFold models of a truncated SKR-1 dimer (amino acids 1 to 83, GGSG, and 96 to 143) and a truncated SKR-1 dimer with C-terminal helices (amino acids 1 to 83, GGSG, and 96 to 176) were produced using ColabFold (*42, 43*) and were superimposed into the NMR structure of a truncated *Dictyostelium discoideum* Skp1A homodimer (Protein Data Bank 6V88) (*39*) using ChimeraX (*79*).

Size exclusion chromatography and multiangle light scattering

Recombinant SKR-1 proteins (0.1 mg/ml) and SYP/SKR-1 complexes (0.1 mg/ml) were separated on Superdex 200 10/300 GL and Superose 6 10/300 GL columns (Cytiva), respectively, that were equilibrated with 10 mM Hepes, 400 mM NaCl, 0.5 mM EGTA, 5 mM $MgCl_2$, 2 mM tris(2-carboxyethyl)phosphine (TCEP), and 5% glycerol at a flow rate of 0.1 ml/min. The light scattering and reflective index profiles of recombinant SKR-1 proteins were collected by miniDAWN and OptiLab (Wyatt Technology). Data were collected every second and analyzed by ASTRA 8 (Wyatt Technology). Bovine serum albumin (Sigma-Aldrich, P0834) was used to calibrate the light scattering detector.

Supplementary Materials

This PDF file includes:

Figs. S1 to S9

Tables S1 to S6

REFERENCES AND NOTES

1. A. Pyatnitskaya, J. Andreani, R. Guérois, A. De Muyt, V. Borde, The Zip4 protein directly couples meiotic crossover formation to synaptonemal complex assembly. *Genes Dev.* **36**, 53–69 (2022).
2. L. Zhang, S. Köhler, R. Rillo-Bohn, A. F. Dernburg, A compartmentalized signaling network mediates crossover control in meiosis. *eLife* **7**, e30789 (2018).

3. D. E. Libuda, S. Uzawa, B. J. Meyer, A. M. Villeneuve, Meiotic chromosome structures constrain and respond to designation of crossover sites. *Nature* **502**, 703–706 (2013).
4. L. Capilla-Pérez, S. Durand, A. Hurel, Q. Lian, A. Chambon, C. Taochy, V. Solier, M. Grelon, R. Mercier, The synaptonemal complex imposes crossover interference and heterochiasmy in *Arabidopsis*. *Proc. Natl. Acad. Sci. U.S.A.* **118**, e2023613118 (2021).
5. M. G. France, J. Enderle, S. Röhrig, H. Puchta, F. C. H. Franklin, J. D. Higgins, ZYP1 is required for obligate cross-over formation and cross-over interference in *Arabidopsis*. *Proc. Natl. Acad. Sci. U.S.A.* **118**, e2021671118 (2021).
6. D. Zickler, N. Kleckner, Meiotic chromosomes: Integrating structure and function. *Annu. Rev. Genet.* **33**, 603–754 (1999).
7. L. E. Kursel, H. D. Cope, O. Rog, Unconventional conservation reveals structure-function relationships in the synaptonemal complex. *eLife* **10**, e72061 (2021).
8. L. W. Hemmer, J. P. Blumenstiel, Holding it together: Rapid evolution and positive selection in the synaptonemal complex of *Drosophila*. *BMC Evol. Biol.* **16**, 91 (2016).
9. M. E. Hurlock, I. Čavka, L. E. Kursel, J. Haversat, M. Wooten, Z. Nizami, R. Turniansky, P. Hoess, J. Ries, J. G. Gall, O. Rog, S. Köhler, Y. Kim, Identification of novel synaptonemal complex components in *C. elegans*. *J. Cell Biol.* **219**, e201910043 (2020).
10. Z. Zhang, S. Xie, R. Wang, S. Guo, Q. Zhao, H. Nie, Y. Liu, F. Zhang, M. Chen, L. Liu, X. Meng, M. Liu, L. Zhao, M. P. Colaiácovo, J. Zhou, J. Gao, Multivalent weak interactions between assembly units drive synaptonemal complex formation. *J. Cell Biol.* **219**, e201910086 (2020).
11. M. P. Colaiácovo, A. J. MacQueen, E. Martinez-Perez, K. McDonald, A. Adamo, A. La Volpe, A. M. Villeneuve, Synaptonemal complex assembly in *C. elegans* is dispensable for loading strand-exchange proteins but critical for proper completion of recombination. *Dev. Cell* **5**, 463–474 (2003).
12. A. J. MacQueen, M. P. Colaiácovo, K. McDonald, A. M. Villeneuve, Synapsis-dependent and -independent mechanisms stabilize homolog pairing during meiotic prophase in *C. elegans*. *Genes Dev.* **16**, 2428–2442 (2002).
13. S. Smolikov, K. Schild-Prüfert, M. P. Colaiácovo, A yeast two-hybrid screen for SYP-3 interactors identifies SYP-4, a component required for synaptonemal complex assembly and chiasma formation in *Caenorhabditis elegans* meiosis. *PLOS Genet.* **5**, e1000669 (2009).
14. S. Smolikov, A. Eizinger, K. Schild-Prufert, A. Hurlburt, K. McDonald, J. Engebrecht, A. M. Villeneuve, M. P. Colaiácovo, SYP-3 restricts synaptonemal complex assembly to bridge paired chromosome axes during meiosis in *Caenorhabditis elegans*. *Genetics* **176**, 2015–2025 (2007).
15. S. G. Gordon, L. E. Kursel, K. Xu, O. Rog, Synaptonemal complex dimerization regulates chromosome alignment and crossover patterning in meiosis. *PLOS Genet.* **17**, e1009205 (2021).
16. M. D. Petroski, R. J. Deshaies, Function and regulation of cullin-RING ubiquitin ligases. *Nat. Rev. Mol. Cell Biol.* **6**, 9–20 (2005).
17. Y. Guan, H. Lin, N. A. Leu, G. Ruthel, S. Y. Fuchs, L. Busino, M. Luo, P. J. Wang, SCF ubiquitin E3 ligase regulates DNA double-strand breaks in early meiotic recombination. *Nucleic Acids Res.* **50**, 5129–5144 (2022).
18. P. Barbosa, L. Zhaunova, S. Debilio, V. Steccanella, V. Kelly, T. Ly, H. Ohkura, SCF-Fbxo42 promotes synaptonemal complex assembly by downregulating PP2A-B56. *J. Cell Biol.* **220**, e202009167 (2021).
19. Z. Zhu, M. Bani Ismail, M. Shinohara, A. Shinohara, SCF^{Cdc4} ubiquitin ligase regulates synaptonemal complex formation during meiosis. *Life Sci. Alliance* **4**, e202000933 (2021).
20. Y. Wang, H. Wu, G. Liang, M. Yang, Defects in nucleolar migration and synapsis in male prophase I in the *ask1-1* mutant of *Arabidopsis*. *Sex. Plant Reprod.* **16**, 273–282 (2004).
21. D. Zhao, X. Yang, L. Quan, L. Timofejeva, N. W. Rigel, H. Ma, C. A. Makaroff, ASK1, a SKP1 homolog, is required for nuclear reorganization, presynaptic homolog juxtaposition and the proper distribution of cohesin during meiosis in *Arabidopsis*. *Plant Mol. Biol.* **62**, 99–110 (2006).
22. N. Tanno, K. Takemoto, Y. Takada-Horisawa, R. Shimada, S. Fujimura, N. Tani, N. Takeda, K. Araki, K.-I. Ishiguro, FBXO47 is essential for preventing the synaptonemal complex from premature disassembly in mouse male meiosis. *iScience* **25**, 104008 (2022).
23. Y. Wang, W.-Y. Gao, L.-L. Wang, R.-L. Wang, Z.-X. Yang, F.-Q. Luo, Y.-H. He, Z.-B. Wang, F.-Q. Wang, Q.-Y. Sun, J. Li, D. Zhang, FBXW24 controls female meiotic prophase progression by regulating SYCP3 ubiquitination. *Clin. Transl. Med.* **12**, e891 (2022).
24. F. Zhang, D. Tang, Y. Shen, Z. Xue, W. Shi, L. Ren, G. Du, Y. Li, Z. Cheng, The F-box protein ZYGO1 mediates bouquet formation to promote homologous pairing, synapsis, and recombination in rice meiosis. *Plant Cell* **29**, 2597–2609 (2017).
25. R. Hua, H. Wei, C. Liu, Y. Zhang, S. Liu, Y. Guo, Y. Cui, X. Zhang, X. Guo, W. Li, M. Liu, FBXO47 regulates telomere-inner nuclear envelope integration by stabilizing TRF2 during meiosis. *Nucleic Acids Res.* **47**, 11755–11770 (2019).
26. A. Mohammad, K. Vanden Broek, C. Wang, A. Daryabeigi, V. Jantsch, D. Hansen, T. Schedl, Initiation of meiotic development is controlled by three post-transcriptional pathways in *Caenorhabditis elegans*. *Genetics* **209**, 1197–1224 (2018).
27. A. Baudrimont, D. Paouneskou, A. Mohammad, R. Lichtenberger, J. Blundon, Y. Kim, M. Hartl, S. Falk, T. Schedl, V. Jantsch, Release of CHK-2 from PPM-1.D anchorage schedules meiotic entry. *Sci. Adv.* **8**, eabl8861 (2022).
28. V. Jantsch, L. Tang, P. Pasierbek, A. Penkner, S. Nayak, A. Baudrimont, T. Schedl, A. Gartner, J. Loidl, *Caenorhabditis elegans* prom-1 is required for meiotic prophase progression and homologous chromosome pairing. *Mol. Biol. Cell* **18**, 4911–4920 (2007).
29. E. Kisielnicka, R. Minasaki, C. R. Eckmann, MAPK signaling couples SCF-mediated degradation of translational regulators to oocyte meiotic progression. *Proc. Natl. Acad. Sci. U.S.A.* **115**, E2772–E2781 (2018).
30. C. A. Spike, G. Huelgas-Morales, T. Tsukamoto, D. Greenstein, Multiple mechanisms inactivate the LIN-41 RNA-binding protein to ensure a robust oocyte-to-embryo transition in *Caenorhabditis elegans*. *Genetics* **210**, 1011–1037 (2018).
31. S. Nayak, F. E. Santiago, H. Jin, D. Lin, T. Schedl, E. T. Kipreos, The *Caenorhabditis elegans* Skp1-related gene family: Diverse functions in cell proliferation, morphogenesis, and meiosis. *Curr. Biol.* **12**, 277–287 (2002).
32. A. Yamanaka, M. Yada, H. Imaki, M. Koga, Y. Ohshima, K.-I. Nakayama, Multiple Skp1-related proteins in *Caenorhabditis elegans*: Diverse patterns of interaction with Cullins and F-box proteins. *Curr. Biol.* **12**, 267–275 (2002).
33. D. J. Killian, E. Harvey, P. Johnson, M. Otori, S. Mitani, D. Xue, SKR-1, a homolog of Skp1 and a member of the SCF(SEL-10) complex, regulates sex-determination and LIN-12/Notch signaling in *C. elegans*. *Dev. Biol.* **322**, 322–331 (2008).
34. B. A. Schulman, A. C. Carrano, P. D. Jeffrey, Z. Bowen, E. R. Kinnucan, M. S. Finnin, S. J. Elledge, J. W. Harper, M. Pagano, N. P. Pavletich, Insights into SCF ubiquitin ligases from the structure of the Skp1-Skp2 complex. *Nature* **408**, 381–386 (2000).
35. N. Zheng, B. A. Schulman, L. Song, J. J. Miller, P. D. Jeffrey, P. Wang, C. Chu, D. M. Koepp, S. J. Elledge, M. Pagano, R. C. Conaway, J. W. Conaway, J. W. Harper, N. P. Pavletich, Structure of the Cul1–Rbx1–Skp1–F boxSkp2 SCF ubiquitin ligase complex. *Nature* **416**, 703–709 (2002).
36. S. Köhler, M. Wojcik, K. Xu, A. F. Dernburg, Superresolution microscopy reveals the three-dimensional organization of meiotic chromosome axes in intact tissue *Caenorhabditis elegans* tissue. *Proc. Natl. Acad. Sci. U.S.A.* **114**, E4734–E4743 (2017).
37. C.-W. Wu, A. Deonarine, A. Przybysz, K. Strange, K. P. Choe, The Skp1 homologs SKR-1/2 are required for the *Caenorhabditis elegans* SKN-1 antioxidant/detoxification response independently of p38 MAPK. *PLOS Genet.* **12**, e1006361 (2016).
38. E. T. Kipreos, L. E. Lander, J. P. Wing, W. W. He, E. M. Hedgecock, *Cul-1* is required for cell cycle exit in *C. elegans* and identifies a novel gene family. *Cell* **85**, 829–839 (1996).
39. H. W. Kim, A. Eletsky, K. J. Gonzalez, H. van der Wel, E.-M. Strauch, J. H. Prestegard, C. M. West, Skp1 dimerization conceals its F-box protein binding site. *Biochemistry* **59**, 1527–1536 (2020).
40. M. T. Henzl, I. Thalmann, R. Thalmann, OCP2 exists as a dimer in the organ of Corti. *Hear. Res.* **126**, 37–46 (1998).
41. M. O. Sheikh, C. M. Schafer, J. T. Powell, K. K. Rodgers, B. H. M. Mooers, C. M. West, Glycosylation of Skp1 affects its conformation and promotes binding to a model F-box protein. *Biochemistry* **53**, 1657–1669 (2014).
42. J. Jumper, R. Evans, A. Pritzel, T. Green, M. Figurnov, O. Ronneberger, K. Tunyasuvunakool, R. Bates, A. Žídek, A. Potapenko, A. Bridgland, C. Meyer, S. A. A. Kohl, A. J. Ballard, A. Cowie, B. Romera-Paredes, S. Nikolov, R. Jain, J. Adler, T. Back, S. Petersen, D. Reiman, E. Clancy, M. Zielinski, M. Steinegger, M. Pacholska, T. Berghammer, S. Bodenstein, D. Silver, O. Vinyals, A. W. Senior, K. Kavukcuoglu, P. Kohli, D. Hassabis, Highly accurate protein structure prediction with AlphaFold. *Nature* **596**, 583–589 (2021).
43. M. Mirdita, K. Schütze, Y. Moriwaki, L. Heo, S. Ovchinnikov, M. Steinegger, ColabFold: Making protein folding accessible to all. *Nat. Methods* **19**, 679–682 (2022).
44. J. Hodgkin, H. R. Horvitz, S. Brenner, Nondisjunction mutants of the nematode *CAENORHABDITIS ELEGANS*. *Genetics* **91**, 67–94 (1979).
45. C. Connelly, P. Hieter, Budding yeast SKP1 encodes an evolutionarily conserved kinetochore protein required for cell cycle progression. *Cell* **86**, 275–285 (1996).
46. J. M. Reitsma, X. Liu, K. M. Reichermeier, A. Moradian, M. J. Sweredoski, S. Hess, R. J. Deshaies, Composition and regulation of the cellular repertoire of SCF ubiquitin ligases. *Cell* **171**, 1326–1339.e14 (2017).
47. N. W. Pierce, J. E. Lee, X. Liu, M. J. Sweredoski, R. L. J. Graham, E. A. Larimore, M. Rome, N. Zheng, B. E. Clurman, S. Hess, S.-O. Shan, R. J. Deshaies, Cand1 promotes assembly of new SCF complexes through dynamic exchange of F box proteins. *Cell* **153**, 206–215 (2013).
48. A. Tan, J. J. Tanner, M. T. Henzl, Energetics of OCP1-OCP2 complex formation. *Biophys. Chem.* **134**, 64–71 (2008).
49. O. Rog, S. Köhler, A. F. Dernburg, The synaptonemal complex has liquid crystalline properties and spatially regulates meiotic recombination factors. *eLife* **6**, e21455 (2017).
50. P. Beltrao, V. Albanèse, L. R. Kenner, D. L. Swaney, A. Burlingame, J. Villén, W. A. Lim, J. S. Fraser, J. Frydman, N. J. Krogan, Systematic functional prioritization of protein posttranslational modifications. *Cell* **150**, 413–425 (2012).
51. P. Meraldi, A. D. McAinsh, E. Rheinbay, P. K. Sorger, Phylogenetic and structural analysis of centromeric DNA and kinetochore proteins. *Genome Biol.* **7**, R23 (2006).
52. O. Stemmann, J. Lechner, The Saccharomyces cerevisiae kinetochore contains a cyclin-CDK complexing homologue, as identified by in vitro reconstitution. *EMBO J.* **15**, 3611–3620 (1996).

53. K. Yan, Z. Zhang, J. Yang, S. H. McLaughlin, D. Barford, Architecture of the CBF3-centromere complex of the budding yeast kinetochore. *Nat. Struct. Mol. Biol.* **25**, 1103–1110 (2018).
54. V. Leber, A. Nans, M. R. Singleton, Structural basis for assembly of the CBF3 kinetochore complex. *EMBO J.* **37**, 269–281 (2018).
55. I. D. Russell, A. S. Grancell, P. K. Sorger, The unstable F-box protein p58-Ctf13 forms the structural core of the CBF3 kinetochore complex. *J. Cell Biol.* **145**, 933–950 (1999).
56. K. B. Kaplan, A. A. Hyman, P. K. Sorger, Regulating the yeast kinetochore by ubiquitin-dependent degradation and Skp1p-mediated phosphorylation. *Cell* **91**, 491–500 (1997).
57. H. Kong, J. Leebens-Mack, W. Ni, C. W. dePamphilis, H. Ma, Highly heterogeneous rates of evolution in the SKP1 gene family in plants and animals: Functional and evolutionary implications. *Mol. Biol. Evol.* **21**, 117–128 (2004).
58. S. Brenner, The genetics of *Caenorhabditis elegans*. *Genetics* **77**, 71–94 (1974).
59. M. Han, G. Wei, C. E. McManus, L. W. Hillier, V. Reinke, Isolated *C. elegans* germ nuclei exhibit distinct genomic profiles of histone modification and gene expression. *BMC Genomics* **20**, 500 (2019).
60. R. S. Kamath, A. G. Fraser, Y. Dong, G. Poulin, R. Durbin, M. Gotta, A. Kanapin, N. Le Bot, S. Moreno, M. Sohrmann, D. P. Welchman, P. Zipperlen, J. Ahringer, Systematic functional analysis of the *Caenorhabditis elegans* genome using RNAi. *Nature* **421**, 231–237 (2003).
61. J.-F. Rual, J. Ceron, J. Koreth, T. Hao, A.-S. Nicot, T. Hirozane-Kishikawa, J. Vandenhaute, S. H. Orkin, D. E. Hill, S. van den Heuvel, M. Vidal, Toward improving *Caenorhabditis elegans* phenome mapping with an ORFeome-based RNAi library. *Genome Res.* **14**, 2162–2168 (2004).
62. I. Čavka, R. M. Power, D. Walsh, T. Zimmermann, S. Köhler, Super-resolution microscopy of the synaptonemal complex within the *Caenorhabditis elegans* germline. *J. Vis. Exp.* 10.3791/64363 , (2022).
63. A. J. MacQueen, C. M. Phillips, N. Bhalla, P. Weiser, A. M. Villeneuve, A. F. Dernburg, Chromosome sites play dual roles to establish homologous synapsis during meiosis in *C. elegans*. *Cell* **123**, 1037–1050 (2005).
64. P. Hoess, M. Mund, M. Reitberger, J. Ries, Dual-color and 3D super-resolution microscopy of multi-protein assemblies. *Methods Mol. Biol.* **1764**, 237–251 (2018).
65. R. Diekmann, M. Kahnwald, A. Schoenit, J. Deschamps, U. Matti, J. Ries, Optimizing imaging speed and excitation intensity for single-molecule localization microscopy. *Nat. Methods* **17**, 909–912 (2020).
66. J. Deschamps, A. Rowald, J. Ries, Efficient homogeneous illumination and optical sectioning for quantitative single-molecule localization microscopy. *Opt. Express* **24**, 28080–28090 (2016).
67. M. Mund, J. A. van der Beek, J. Deschamps, S. Dmitrieff, P. Hoess, J. L. Monster, A. Picco, F. Nédélec, M. Kaksonen, J. Ries, Systematic nanoscale analysis of endocytosis links efficient vesicle formation to patterned actin nucleation. *Cell* **174**, 884–896.e17 (2018).
68. D. Schröder, J. Deschamps, A. Dasgupta, U. Matti, J. Ries, Cost-efficient open source laser engine for microscopy. *Biomed. Opt. Express* **11**, 609–623 (2020).
69. M. Mund, A. Tschanz, Y.-L. Wu, F. Frey, J. L. Mehl, M. Kaksonen, O. Avinoam, U. S. Schwarz, J. Ries, Clathrin coats partially preassemble and subsequently bend during endocytosis. *J. Cell Biol.* **222**, e202206038 (2023).
70. Y. Li, W. Shi, S. Liu, I. Cavka, Y.-L. Wu, U. Matti, D. Wu, S. Koehler, J. Ries, Global fitting for high-accuracy multi-channel single-molecule localization. *Nat. Commun.* **13**, 3133 (2022).
71. J. Deschamps, C. Kieser, P. Hoess, T. Deguchi, J. Ries, MicroFPGA: An affordable FPGA platform for microscope control. *HardwareX* **13**, e00407 (2023).
72. J. Deschamps, J. Ries, EMU: Reconfigurable graphical user interfaces for micro-manager. *BMC Bioinformatics* **21**, 456 (2020).
73. A. D. Edelstein, M. A. Tsuchida, N. Amodaj, H. Pinkard, R. D. Vale, N. Stuurman, Advanced methods of microscope control using μManager software. *J. Biol. Methods* **1**, e10 (2014).
74. A. Edelstein, N. Amodaj, K. Hoover, R. Vale, N. Stuurman, Computer control of microscopes using μManager. *Curr. Protoc. Mol. Biol.* **92**, 14.20.1–14.20.17 (2010).
75. J. Ries, SMAP: A modular super-resolution microscopy analysis platform for SMLM data. *Nat. Methods* **17**, 870–872 (2020).
76. Y. Li, M. Mund, P. Hoess, J. Deschamps, U. Matti, B. Nijmeijer, V. J. Sabinina, J. Ellenberg, I. Schoen, J. Ries, Real-time 3D single-molecule localization using experimental point spread functions. *Nat. Methods* **15**, 367–369 (2018).
77. R. P. J. Nieuwenhuizen, K. A. Lidke, M. Bates, D. L. Puig, D. Grünwald, S. Stallinga, B. Rieger, Measuring image resolution in optical nanoscopy. *Nat. Methods* **10**, 557–562 (2013).
78. N. Banterle, K. H. Bui, E. A. Lemke, M. Beck, Fourier ring correlation as a resolution criterion for super-resolution microscopy. *J. Struct. Biol.* **183**, 363–367 (2013).
79. E. C. Meng, T. D. Goddard, E. F. Pettersen, G. S. Couch, Z. J. Pearson, J. H. Morris, T. E. Ferrin, UCSF ChimeraX: Tools for structure building and analysis. *Protein Sci.* **32**, e4792 (2023).

Acknowledgments: We thank B. Cole in the Mass Spectrometry and Proteomics Facility at Johns Hopkins School of Medicine for mass spectrometry analysis, B. Traina (Juniata College, Huntingdon, PA) for the assistance in plasmid construction, and J. Kim (Johns Hopkins University, Baltimore, MD) for the *C. elegans* RNAi libraries and critical reading of the manuscript. Some strains were provided by the *Caenorhabditis* Genetics Center, which is funded by the National Institutes of Health Office of Research Infrastructure Programs (P40 OD010440). **Funding:** This work was supported by National Institutes of Health (R35GM124895 to Y.K.), National Institutes of Health Predoctoral Fellowship (F31HD100142 to J.H.), and European Molecular Biology Laboratory (to I.Č. and S.K.). **Author contributions:** Conceptualization: J.M.B., B.I.C., and Y.K. Methodology: J.M.B., B.I.C., J.W.B., I.Č., J.H., J.R., S.K., and Y.K. Resources: J.M.B., J.R., and Y.K. Investigation: J.M.B., B.I.C., J.W.B., I.Č., J.H., and Y.K. Validation: J.M.B., B.I.C., I.Č., and Y.K. Formal analysis: J.M.B., B.I.C., I.Č., and Y.K. Visualization: J.M.B., B.I.C., J.H., I.Č., S.K., and Y.K. Supervision: J.M.B., B.I.C., Y.K., J.R., and S.K. Data curation: J.M.B. and J.R. Software: J.R. Funding acquisition: Y.K. and S.K. Project administration: J.M.B., B.I.C., and Y.K. Writing (original draft): J.M.B., B.I.C., S.K., and Y.K. Writing (review and editing): J.M.B., B.I.C., S.K., and Y.K. **Competing interests:** The authors declare that they have no competing interests. **Data and materials availability:** All data needed to evaluate the conclusions of this paper are present in the paper and/or the Supplementary Materials. Requests for strains generated in this study should be submitted to Y.K.

Submitted 20 October 2023
Accepted 12 January 2024
Published 14 February 2024
10.1126/sciadv.adl4876